nature energy

Article

https://doi.org/10.1038/s41560-024-01473-2

Quadruple the rate capability of high-energy batteries through a porous current collector design

Received: 11 April 2023

Accepted: 29 January 2024

Yusheng Ye[1,7], **Rong Xu**[1,7], **Wenxiao Huang**[1], **Huayue Ai**[2], **Wenbo Zhang**[1], **Jordan Otto Affeld**[1], **Andy Cui**[1], **Fang Liu**[1], **Xin Gao**[1], **Zhouyi Chen**[1], **Tony Li**[1], **Xin Xiao**[1], **Zewen Zhang**[1], **Yucan Peng**[1], **Rafael A. Vila**[1], **Yecun Wu**[3], **Solomon T. Oyakhire**[4], **Hideaki Kuwajima**[5], **Yoshiaki Suzuki**[5], **Ryuhei Matsumoto**[5], **Yasuyuki Masuda**[5], **Takahiro Yuuki**[5], **Yuri Nakayama**[5] & **Yi Cui**[1,6] ✉

Achieving extremely fast charging yet maintaining high energy density remains a challenge in the battery field. Traditional current collectors, being impermeable to electrolytes, hinder the movement of Li^+ ions and restrict the high-rate capability of thick electrodes. Here we conceptualize a porous current collector for energy-dense and extremely fast-charging batteries. This porous design allows Li^+ ions to pass through both the current collector and the separator simultaneously, thereby reducing the effective Li^+ transport distance by half and quadrupling the diffusion-limited C-rate capability without compromising the energy density. Multilayer pouch cells equipped with this current collector demonstrate high specific energy (276 Wh kg^{-1}) and remarkable fast-charging capabilities at rates of 4 C (78.3% state of charge), 6 C (70.5% state of charge) and 10 C (54.3% state of charge). This porous current collector design is compatible with existing battery manufacturing processes and other fast-charging strategies, enriching battery configurations for designing next-generation batteries.

The widespread adoption of electric vehicles and the realization of electric aircrafts are becoming increasingly reliant on energy-dense lithium-ion batteries (LIBs)[1–4]. The state-of-the-art energy-dense (>250 Wh kg^{-1}) LIBs are composed of nickel-rich layered oxide cathodes and graphite anodes[5]. While achieving a cruising range of over 300 miles for electric vehicles is now feasible through the use of thick electrodes, the issue of long charging time still poses a significant challenge. As a result, extremely fast charging has become one of the most sought-after features to accelerate the widespread adoption and eliminate the 'range anxiety' barrier. This demands a charging time of less than 15 min to reach 80% of state of charge (SOC) from 0% (refs. 6,7).

Diffusion limitation is a key factor that hinders the rate performance of batteries[8]. The length of effective Li^+ pathway within the porous electrode plays a critical role, and it increases with the areal loading. Several strategies have been proposed to address diffusion issues. Thinning electrodes is a primary means to increase rate capability, but it does come at the cost of reducing the energy density of batteries[9,10]. Additionally, other approaches such as electrolyte engineering to accelerate ionic conduction[11,12], thermal modulation to enhance

---

[1]Department of Materials Science and Engineering, Stanford University, Stanford, CA, USA. [2]Department of Chemistry, Stanford University, Stanford, CA, USA. [3]Department of Electrical Engineering, Stanford University, Stanford, CA, USA. [4]Department of Chemical Engineering, Stanford University, Stanford, CA, USA. [5]Murata Manufacturing Co., Ltd, Nagaokakyo-shi, Kyoto, Japan. [6]Stanford Institute for Materials and Energy Sciences, SLAC National Accelerator Laboratory, Menlo Park, CA, USA. [7]These authors contributed equally: Yusheng Ye, Rong Xu. ✉e-mail: yicui@stanford.edu

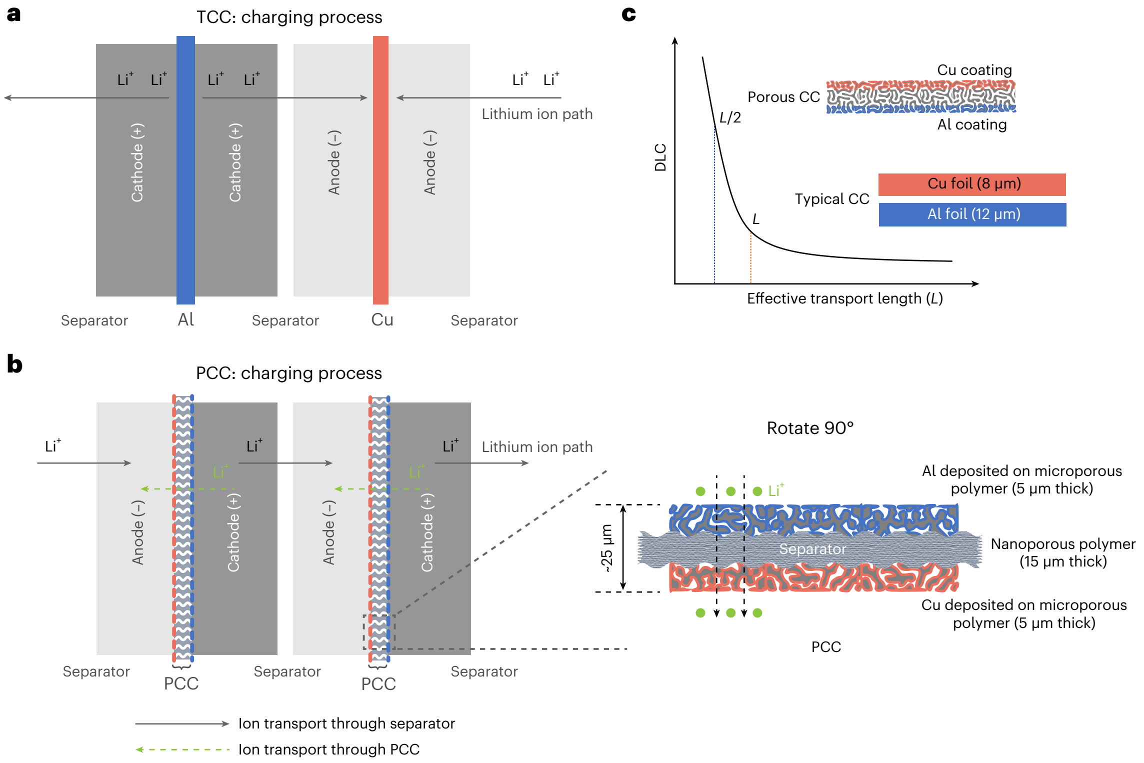

Fig. 1 | The design principle of the PCC in batteries. a,**b**, Multilayer pouch cells with a TCC (**a**) and PCC (**b**). In the TCC case, Li$^+$ transport between electrodes is limited to being only one sided through the separator (indicated by the long arrows in **a**). In the PCC case, Li$^+$ transport occurs on both sides simultaneously, both through PCC and separator (indicated by the short arrows in **a**). The zoomed-in figure shows the schematic of PCC, which consists of a sandwiched, porous and hierarchical polymer matrix coated with two types of metal on the surface. **c**, The conceptual comparison of DLC in TCC and PCC cells. The use of a PCC halves the effective Li$^+$ transport path length, quadrupling the diffusion-limited rate capability of batteries.

Li$^+$ transport[13–15], tortuosity reduction to shorten the path length in electrodes[15,16], and so on, have also been suggested to facilitate Li$^+$ transport in batteries. However, these strategies have trade-offs in terms of electrochemical and/or thermal stability and energy density.

Among various approaches, reducing the effective Li$^+$ transport length could have the most profound effect on increasing rate capability. As indicated by equation (1), the diffusion-limited C rate (DLC) describes the maximum rate at which the Li$^+$ ions can diffuse through the electrode and the electrolyte to engage in the electrochemical reaction. This occurs when the Li$^+$ concentration near the current collector reaches zero[16]. DLC is inversely proportional to the square root of effective electrode thickness. Operating above DLC rate causes depletion of Li$^+$ at a specific depth within the electrode, rendering the active materials beyond that point unusable[6,17]. Additionally, high C rates result in the increased polarization, causing the anode potential to drop below the Li$^+$/Li^0 equilibrium potential. This can lead to the formation of metallic lithium (Li^0) deposits on the anode surface, known as Li^0 plating[18]. In the best-case scenario, these effects compromise the deployable energy density, reversibility and lifespan of batteries. In worst-case scenario, they can trigger thermal runaway and explosion[19].

$$\mathrm{DLC} = \frac{2zFD\varepsilon^{\gamma} c^{0}_{\mathrm{Li+}}}{\omega\rho Q_{\mathrm{m}}(1-\varepsilon)L^{2}}, \tag{1}$$

where $z, F, D, \varepsilon, \gamma\, c^0_{\mathrm{Li+}}, \omega, \rho, Q_\mathrm{m}$ and L are the valence, the Faraday constant, diffusivity, porosity, tortuosity factor, the initial Li-ion concentration in the electrolyte, the mass fraction of the active material, the apparent density of the composite, the gravimetric capacity of the active material, and the thickness of the electrode layer, respectively.

After reevaluating the commonly used battery architecture, we found that the importance of current collectors have long been overlooked. Traditional current collectors (TCC), such as solid metal foils including Cu and Al, lack porosity and are impermeable to electrolyte (Fig. 1a)[20]. Consequently, these TCC do not contribute to Li$^+$ transport and restrict the Li$^+$ transport between electrodes to being only one sided.

Here, we conceptualize a thin (25 µm) and porous current collector (PCC) that can regulate Li$^+$ movement through both current collector and separator, for high-energy batteries (Fig. 1b). The current collector is composed of a sandwiched, porous and hierarchical polymer matrix coated with roughly 1.5 µm thick cathodic and anodic conductive metal on each side, respectively. Comparing Fig. 1a,b, we would identify one critical change on the configuration of battery cells. While the thickness of each electrode layer is identical for both cases, the arrangement of anodes and cathodes is changed from alternating every two layers (cathode–cathode–anode–anode) to alternating every single layer (cathode–anode–cathode–anode). This modification maintains the necessary electrode thickness for achieving high energy density for both cases. However, in the PCC case, the effective Li$^+$ transport path length is reduced to one half of the traditional battery configuration. As conceptually shown in Fig. 1c, this reduction in effective diffusion length results in a fourfold increase in the diffusion-limited rate capability. Multilayer pouch cells equipped with this PCC, with a high areal cathode loading of 3 mAh cm^{-2}, exhibit a specific energy of approximately 276 Wh kg^{-1} at the whole-cell level. Additionally, these cells demonstrate remarkable rate capabilities: reaching 4 C (15 min charging, from 0 to 78.3% SOC), 6 C (10 min charging, from 0 to 70.5% SOC) and 10 C (6 min charging, from 0 to 54.3% SOC). This design reforms the traditional battery structure, enabling the use of thick electrodes for energy-dense batteries while concurrently achieving high-rate capability.

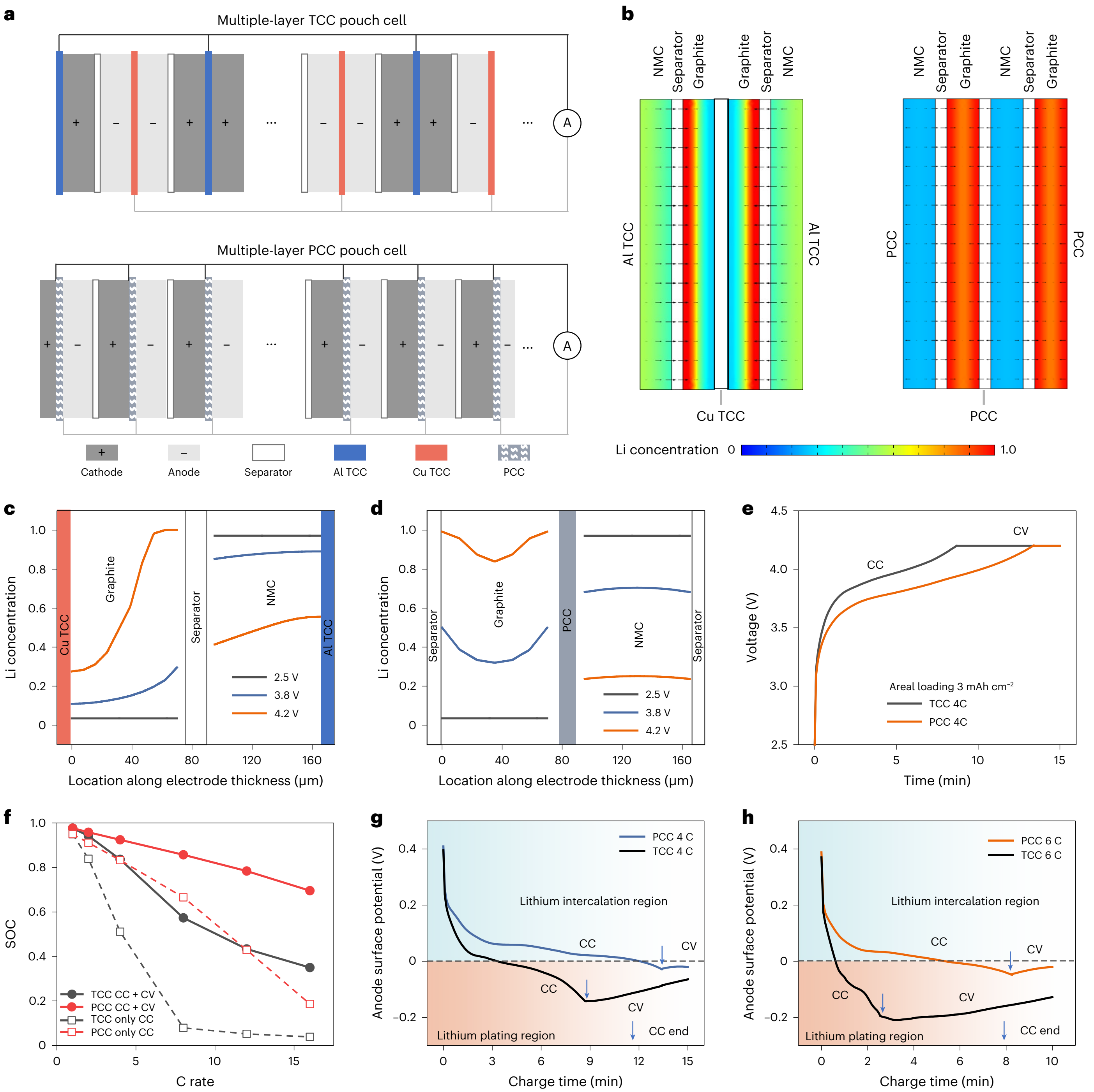

Fig. 2 | Numerical simulation of batteries with a TCC and PCC. a, Multilayer pouch cell configuration with a TCC and PCC. **b**, The lithium concentration map of electrodes in two battery units when charged to the cutoff voltage of 4.2 V. **c**,**d**, Distribution of lithium concentration in the TCC case (**c**) and PCC case (**d**) along the direction of electrode thickness at different charging voltages (2.5, 3.8 and 4.2 V). **e**, Charge curves of TCC and PCC batteries at 4 C, with total charging time controlled at 15 min. **f**, Normalized capacity of batteries with TCC and PCC under different charging protocols. **g**,**h**, Evolution of the electrode potential E_{ct} at the anode surface near the separator when charging at 4 C (**g**) and 6 C (**h**). NMC, lithium nickel manganese cobalt oxide ($LiNi_{0.5}Mn_{0.3}Co_{0.2}O_2$).

The proof-of-concept of PCC by numerical simulation

We selected a typical high-energy battery to illustrate our concept, consisted of lithium nickel manganese cobalt oxide ($LiNi_{0.5}Mn_{0.3}Co_{0.2}O_2$, NMC) as the cathode and graphite as the anode. To better understand the electrochemical processes on fast charging, we first performed numerical simulations. In Fig. 2a, we present multilayer pouch cells with TCC and PCC, which demonstrate the cell assembling configuration used in our later demonstration and real-world application. For our experiment, we used galvanostatic charging at a 4 C rate (12 mA cm^{-2}, C rates are based on a NMC cathode with an areal loading of 3 mAh cm^{-2}). The battery was charged to the cutoff voltage of 4.2 V and held at 4.2 V until the total charging time reached 15 min. Figure 2b shows the distributions of lithium concentration in the active materials for two different battery configurations. The deep red (blue) colour indicates a high (low) lithium concentration.

Owing to the Li^+ transport limitation, the lithium concentration of TCC batteries is highly inhomogeneous across the thickness of electrodes. In the left panel of Fig. 2b, it can be observed that graphite particles near the separator have a higher lithium concentration of approximately 1.0, while those farther away from the separator have a lower value of around 0.3. In the cathode, the NMC particles also exhibit an uneven lithium concentration ranging from 0.4 to 0.6. Previous studies have shown that such non-uniform electrochemical processes in batteries can lead to damage within the active particles and at the interfaces, resulting in irreversible capacity decay on battery cycling[21,22].

Alternatively, Li^+ ions can transport through both the separator and PCC, thereby effectively reducing the effective transport length by one half and significantly reducing the inhomogeneity of lithium distribution. As shown in the right panel of Fig. 2b, the lithium distribution in graphite anode has minimal variation, ranging from a fully lithiated state (lithium concentration of 1.0) at the sides of anode surface to an 80% lithiated state (lithium concentration of 0.8) at the central anode. At the same time, the lithium distribution in the NMC cathode is uniform, with a lithium concentration of approximately 0.34. It is worth noting that the distributions of Li ions in the NMC and graphite differ due to the higher tortuosity of the graphite anode compared to the NMC cathode[23]. Consequently, the transport of Li ions is slower in the graphite anode, resulting in a higher gradient of Li-ion distribution. This more homogeneous use of active materials in batteries with PCC can be observed at different charging status (for example, 2.5, 3.8 and 4.2 V), as depicted in Fig. 2c,d and Supplementary Fig. 1, where the distribution of lithium in the electrodes are plotted along the direction of electrode thickness. As a result, batteries with PCC exhibit lower voltage polarization and higher available capacity compared to batteries with TCC (Fig. 2e). This difference in polarization and available capacity could be further amplified when charging at higher C rates (Fig. 2f) or thicker electrodes (9 mAh cm^{-2}, Supplementary Fig. 2). Figure 2f shows the simulation the SOC for TCC and PCC batteries under two different charging protocols. (1) When charged to the cutoff voltage of 4.2 V using a simple constant current (CC, dashed lines) mode, PCC cells exhibit a significantly higher SOC compared to TCC pouch cells. The maximum improvement in SOC is achieved at a charge rate of 8 C for PCC cells. Beyond this rate, lithium depletion occurs, similar to what is observed in TCC cases but at a much lower C rate. (2) When charged to the cutoff voltage of 4.2 V using a combination of CC and constant voltage (CC-CV, solid line) mode until a specified charge time is reached, the SOC of PCC cells is observed to be significantly higher than that of TCC cells. At a 4 C CC-CV charge mode, PCC cells can reach 92.4% SOC within 15 minutes. At an 8 C CC-CV charge mode, PCC cells can reach 85.7% SOC within 11.6 minutes.

Another challenge in fast charging of batteries is the potential occurrence of Li^0 plating, which often starts from the surface of graphite particles in the anode due to their uneven use[24]. During the fast charging, the graphite particles near the separator rapidly reach a high SOC of 1.0, which can lead to early Li^0 plating. The anode electrode potential can be described as $E_{ct} = \eta_{int} + E_{eq}$, where η_{int} is the overpotential for the Li^+ intercalation into the graphite and E_{eq} is the equilibrium potential for Li intercalation into the graphite. During fast charging, since the graphite particles near the separator quickly reach 100% SOC, the E_{eq} could drop to 0, resulting in the E_{ct} being lower than zero and therefore causing the Li^0 plating on the surface of graphite particles.

To quantitatively compare the possibility of Li^0 plating in the batteries with TCC and PCC, we analysed the evolution of E_{ct} at the anode surface close to the cathode (Fig. 2g,h). It was observed that the E_{ct} gradually drops to low values, and the lowest E_{ct} appears at the end of CC charging. For TCC batteries, the lowest E_{ct} is approximately −0.143 and −0.209 V for the C rates of 4 and 6 C, respectively, indicating the inevitable occurrence of Li^0 plating during battery fast charging. In contrast, for PCC batteries, the E_{ct} for PCC is only −0.029 and −0.049 V for the C rates of 4 and 6 C, respectively, which are lower than the overpotential required for Li^0 nucleation on surface of graphite particles[25]. Additionally, the anode of PCC cell exhibits a more homogeneous distribution across the graphite electrode thickness than the TCC cells, as shown in the spatial distribution of the graphite anode under a charging rate of 4 C (Supplementary Fig. 3). Therefore, we expect batteries with PCC to have a higher tolerance for Li^0 plating and thus offer increased safety during fast charging.

The design and fabrication of PCC

On the basis of our initial analysis, we determined that a PCC design that integrates with the functionalities of current collectors (both cathode and anode) and a separator are necessary to achieve our goals. Therefore, we developed a three-layered, hierarchical and bipolar PCC to meet the requirements (Fig. 3a). To ensure excellent electrochemical stability (Supplementary Fig. 4) and good mechanical properties, we use a bullet-proof, thin and nanoporous Kevlar film (Fig. 3b,c, average pore size 500 nm, porosity 65%, 15 μm thick) as the main substrate of PCC. Kevlar is one of the strongest polymers and is often used as body armour due to its bullet-repellent properties, making it suitable for use as a current collector. Additionally, it separates the two electrodes, preventing potential electrical shorting during battery operation. Subsequently, we coated each side of the Kevlar film with a layer (~5 μm) of microporous polymer by a phase separation method (Methods). We optimized the pore size of surficial coating layers to be around 3–4 μm to meet the criteria of both good electrolyte permeability and thick metal coating thereafter (Fig. 3d,e). If the pore size is too small, the metal coating could block the pore structure and hinder the Li^+ transport (Supplementary Fig. 5).

We then proceeded to coat Cu and Al metal on each side of the abovementioned hybrid PCC matrix, respectively. By applying a sufficiently thick metal coating, the impact of electronic conductivity on cell resistance becomes negligible[26,27]. We optimized the thickness of the metal coating to 1.5 μm to ensure the high electronic conductivity of the PCC. After metal coating, the submicrometre pore size of the surficial layers is maintained, allowing for fast electrolyte permeation through the PCC (Fig. 3f,g). Due to the tortuosity of microporous polymer coating on Kevlar, the conductive metals are only coated on the superficial layer, as confirmed by the cross-sectional scanning electron microscopy (SEM) image (Supplementary Fig. 6) and energy dispersive X-ray spectroscopy analysis (Fig. 3h). Therefore, there is no electronic connection between two sizes of the PCC, and the intermediate Kevlar layer remains unobstructed by the metals. The porosity of PCC plays a crucial role in various aspects of battery performance, including electronic conductivity, ionic conductivity, mechanical stability, thermal behaviour, and electrochemical performance (Supplementary Fig. 7).

Compared to TCC with Cu foil (~120 GPa) and Al foil (~70 GPa), our PCC shows a high Young's modulus of 35.3 GPa (Supplementary Fig. 8) and high electronic conductivity of 4.67×10^7 S m^{-1} (Supplementary Fig. 9). We also conducted the electrical calculation for two battery design using PCC, including typical welding and tab-less configurations (Fig. 3i and Supplementary Fig. 10). The tab-less configuration[28] effectively reduces the current collector resistance in 18650 type cells (3 Ah). In PCC cells with tab-less design, a resistance of below 10 mΩ can be achieved within the practical range of the current collector length (800–1,000 mm).

To evaluate the electrolyte permeability of PCC, we compared the ionic conductivity through blocking cells assembled with different porous films, including polyethylene (Celgard 2500), a triple-layered polyolefin separator (Celgard 2325), a triple-layer PCC polymer matrix (PCC without metal) and a PCC (Fig. 3j and Supplementary Fig. 11). Then, 1 M lithium hexafluorophosphate ($LiPF_6$) in a mixture of ethylene carbonate and ethyl methyl carbonate (3:7 vol%) with 2 wt% fluoroethylene carbonate was used as the electrolyte. It was found that

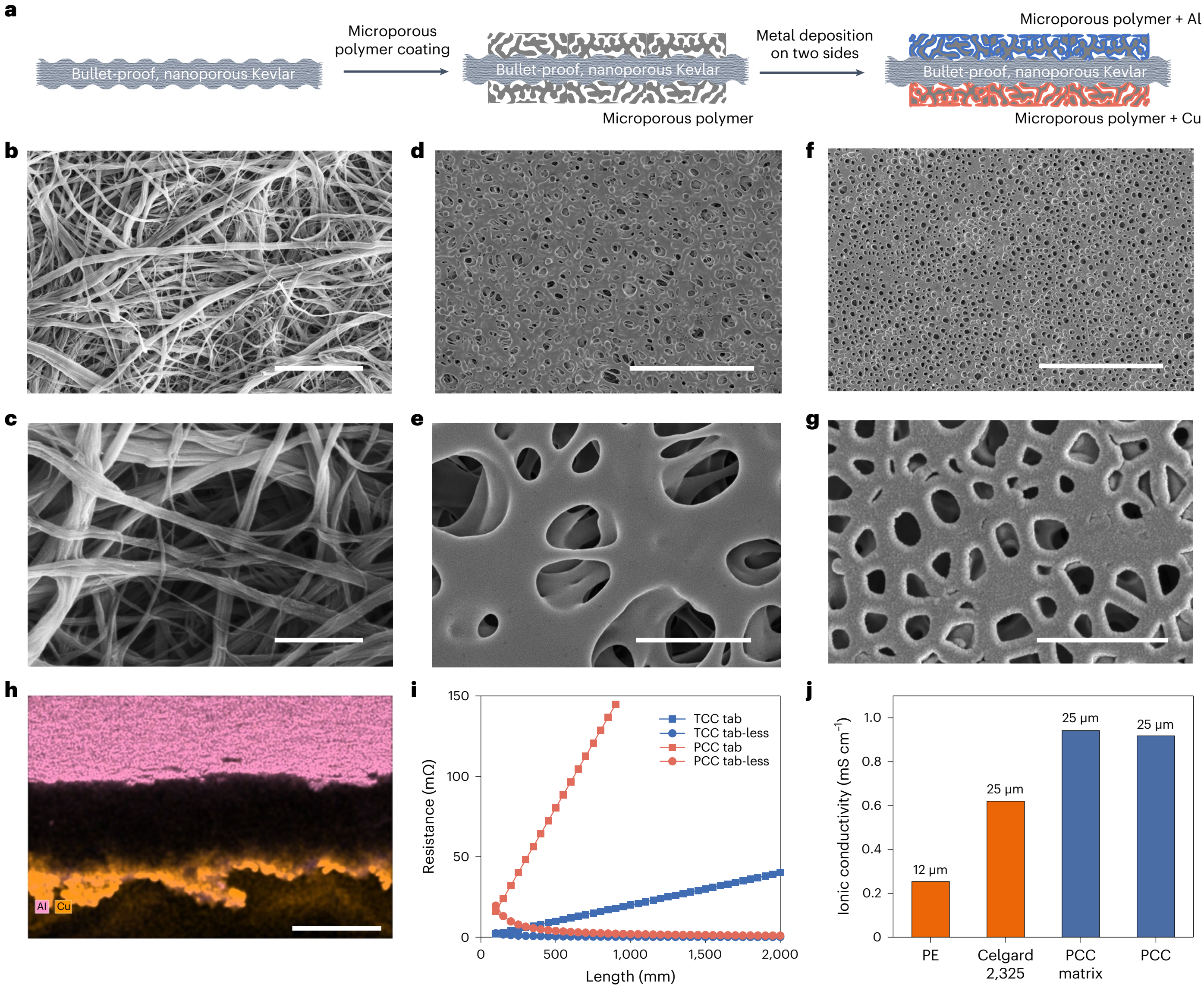

Fig. 3 | The main design concept of the PCC and its properties. **a**, Schematic illustration of the PCC fabrication process. **b**–**g**, The SEM images showing the morphology of the bullet-proof Kevlar film (**b**,**c**), PCC matrix (**d**,**e**) and PCC (**f**,**g**). **h**, Energy dispersive X-ray spectroscopy shows the distribution of metal across the thickness direction of the PCC (SEM image shown in Supplementary Fig. 6). **i**, Variation of current collector resistances as with their lengths. **j**, Comparison of ionic conductivity among commercial separators, PCC matrix and PCC. Scale bars, 5 µm (**b**), 1 µm (**c**), 20 µm (**d**,**f**,**h**) and 3 µm (**e**,**g**).

both a PCC without metal (0.942 mS cm^{-1}) and a PCC (0.918 mS cm^{-1}) exhibited a much higher ionic conductivity compared to commercial polyethylene (0.254 mS cm^{-1}) and Celgard 2325 (0.62 mS cm^{-1}) separators. In our PCC fabrication, the ionic conductivity of the PCC only slightly decreased after metal coating. This can be attributed to several factors: (1) the porosity of the PCC remains well-preserved after metal coating, allowing for fast ion transport and ensuring high ionic conductivity. (2) The metal coatings have minimal impact on the tortuosity of the pores, thereby preserving the ion transport paths. (3) The PCC's electrolyte-philic nature promotes the redistribution of the electrolyte in PCC, minimizing the decrease in ionic conductivity. Additionally, the contact angle of PCC with the electrolyte (~2°) is much smaller than that of a commercial separator (Celgard 2325) with electrolyte (~34°), demonstrating the electrolyte-philic property of the PCC (Supplementary Fig. 12).

Compared to traditional battery configurations with solid foil (7.2 mg cm^{-2} Cu for 8 µm thickness, 3.2 mg cm^{-2} Al for 12 µm thickness) as current collectors, the PCC design significantly reduces the areal weight of current collectors to 2.2 mg cm^{-2}, potentially reducing the 'dead weight' in the battery by approximately 8% at the whole-cell level. It is also worth mentioning that the new PCC concept is a universal design that can be used with different materials of choice. Various conductive coating (such as, carbon nanotubes, porous metal films) and porous film (such as, commercial separators, and poly(vinylidene fluoride-cohexafluoropropylene), PVDF-HFP) could be integrated to construct this hierarchical PCC (Supplementary Fig. 13).

Fast-charging capability of multilayer pouch cells

To fabricate pouch cells with PCC, we incorporated segregated Tuball carbon nanotubes into thick electrodes to achieve high stability (Supplementary Figs. 14 and 15)[29]. These segregated networks contribute to the formation of crack-free electrodes with high areal capacity ranging from 3 to 9 mAh cm^{-2}. The obtained electrodes were then calendered with either TCC or PCC (Supplementary Fig. 16) to assemble multilayer

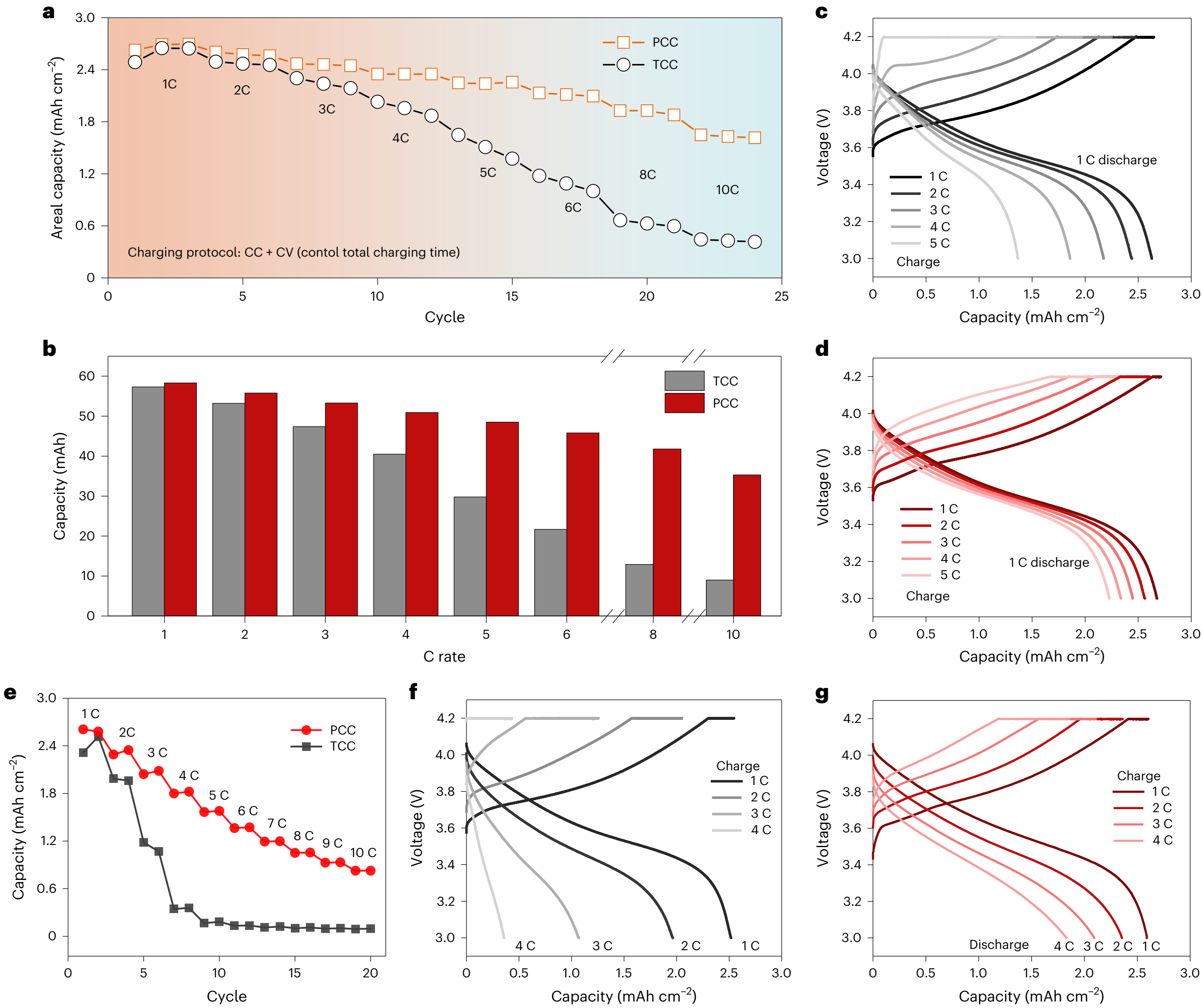

Fig. 4 | Electrochemical performance of multilayer pouch cells with TCC and PCC. a, Rate performance of the multilayer pouch cells with TCC and PCC. **b**, Comparison of the available capacity of the pouch cells after charging at a rate range of 1–10 C by controlling the overall CC-CV charging time. **c**,**d**, Charge and discharge curves of the pouch cells with TCC (**c**) and PCC (**d**). The cells are charged at different rates and discharged at a C rate of 1 C under until a cutoff voltage of 3 V. **e**, Comparison of fast charge and fast discharge capacity comparison of the TCC and PCC pouch cells from 1 to 10 C. **f**,**g**, Charge and discharge curves of the pouch cells with TCC (**f**) and PCC (**g**) at the fast charge and fast discharge protocols.

pouch cells. These cells, with an anode/cathode capacity ratio of 1.1, were combined with Celgard 2325 separator and the aforementioned electrolyte, and subsequently sealed in an aluminium plastic film. Due to the high areal loading (3 mAh cm^{-2}) and the weight reduction from the current collector, the big-size PCC pouch cells can achieve a specific energy density of approximately 276 Wh kg^{-1} (Supplementary Note 1). To evaluate the rate performance, we used an optimized CC-CV protocol in which the total CC and CV charging time reaching a specific point on the basis of the charging rate (1 h for 1 C, 30 min for 2 C and so forth), instead of the typical charging protocols that use a CC-CV mode ended by holding at 4.2 V until reaching a cutoff current of 0.5 C (as mentioned in the paper)[30].

Figure 4a shows the areal discharge capacities of the pouch cells at 1 C after being charged at various C rates, ranging from 1 C (1 h of charging) to 10 C (6 min of charging). To investigate the available capacity after different fast-charging C rates and eliminate any potential 'dead capacity' effect, we discharged the cells completely to 3.0 V at 1 C and compared their deliverable discharge capacities. After 1 C charging, the deliverable discharge capacity of the pouch cells with TCC and PCC is very similar, indicating that the lithium-ion transport is fast enough to participate in the electrochemical reaction in both battery configurations. However, as the charging C rates increase, the capacities of the TCC pouch cell rapidly decrease. Once the charging C rates reach or exceed 3 C (20 min charging), the capacity drops significantly due to severe lithium depletion. Even cycling at the same high C rates, the available discharge capacity for the TCC case continues to decrease due to the generation of irreversible capacity. This decrease in available capacity is mainly attributed to Li^0 plating triggered by a large overpotential, resulting in the generation of 'dead lithium' and the formation of inversible solid electrolyte interphase (SEI), which sacrifices the active capacity[31]. In contrast, the PCC case exhibits a much higher and more stable capacity compared to TCC at high C rates. As shown in

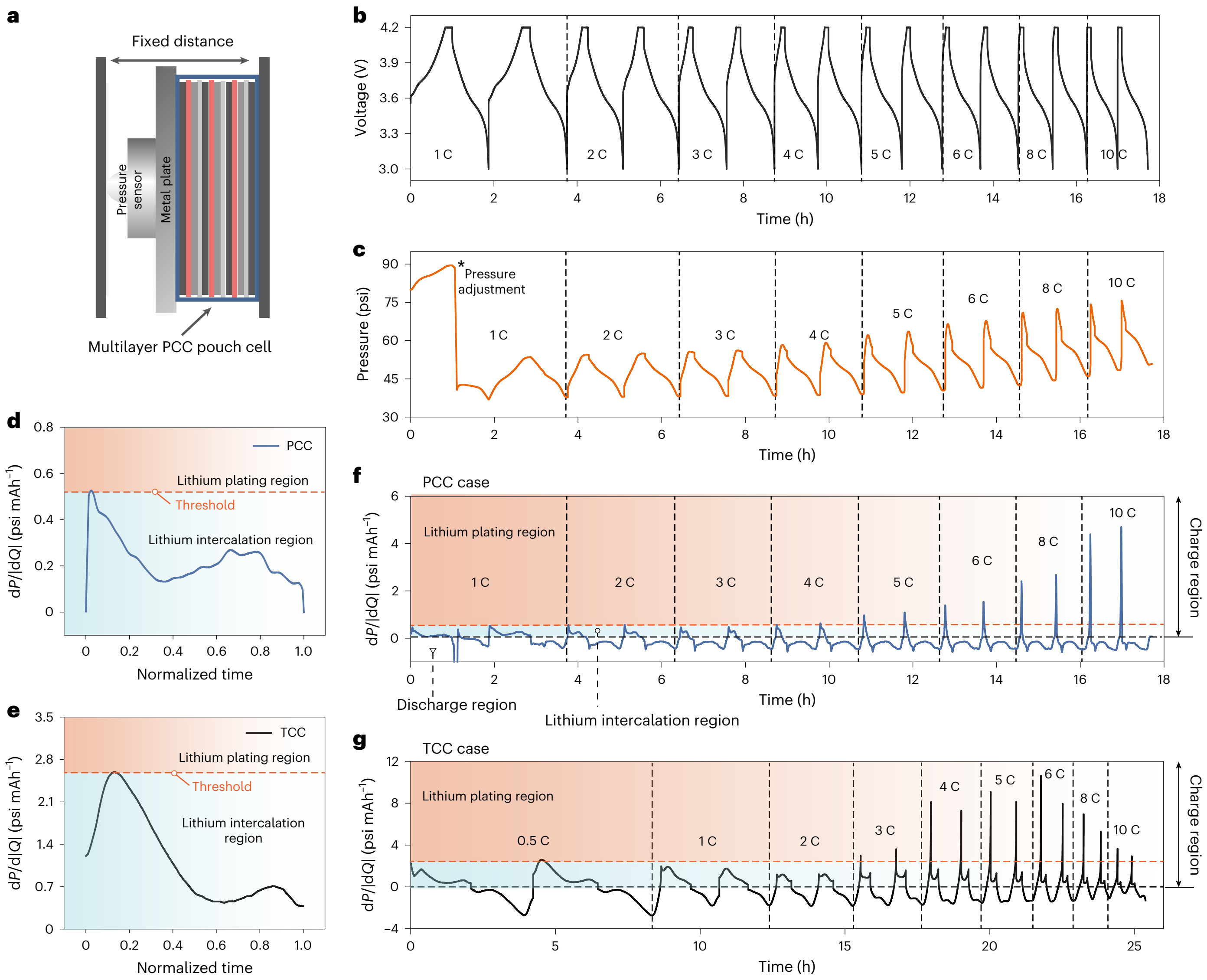

Fig. 5 | DPS reveals the Li^0 plating event during fast charging. **a**, The configuration of in operando pressure measurement on the multilayer pouch cell during extremely fast charging. **b**,**c**, Charge–discharge curve (**b**) and pressure evolution (**c**) of NMC/graphite multilayer pouch cells with PCC cycled at a C rate ranging between 1 and 10 C. Pressure fluctuation in first cycle is caused by the initial pressure adjustment, which does not affect the pressure response thereafter since it does not affect the derivative value of dP/dQ. **d**,**e**, The dP/dQ profiles of the cell charged at slow charging rates to establish the threshold of Li^0 plating of PCC (**d**) and TCC (**e**) cells. The profile goes beyond the threshold indicating Li^0 plating has occurred. **f**,**g**, The dP/dQ profiles of the PCC (**f**) and TCC (**g**) cell charged at different charge–discharge C rates. All the discharged protocols are set to 1 C with a cutoff voltage of 3.0 V. To process the dP/|dQ| data, the resting times after charge and discharge are removed during data analysis.

Fig. 4b, the capacities of the PCC pouch cell at 4 C (15 min charging), 6 C (10 min charging) and 10 C (6 min charging) are 78.3% SOC (62.3% for TCC), 70.5% (33.4% for TCC) and 54.3% (13.8% for TCC), respectively.

Figure 4c,d depicts the charge and discharge curves of the multilayer pouch cells with TCC and PCC. The CC charging portion of the pouch cell with PCC is much longer than that with TCC due to the greatly mediated electrolyte concentration polarization, as also confirmed by the numerical simulation in Fig. 2e. The longer CC charge portion is a crucial indicator of fast-charging capability, as it can contribute to higher capacity. Therefore, the use of PCC significantly enhances the available capacity of cells. As the charging C rate increases from 1 to 5 C, the capacity of the TCC pouch cell decays exponentially, indicating the rapid depletion of Li$^+$ at a specific electrode, beyond which active materials can no longer be used. In contrast, the PCC case shows a near-linear decay trend, suggesting that mass transport does not significantly affect the rate behaviours below 5 C. However, once the C rate exceeds 5 C, the capacity decay rate of the PCC cell accelerates, indicating an increased level of lithium depletion. At higher C rates (>10 C), we anticipate observing rapid capacity decay due to various factors, including increased concentration polarization and particle fracture, among others.

The halving of effective Li$^+$ transport path length also promises fast discharge capability in the multilayer batteries. Therefore, we conducted tests on the fast-discharging performance with a cutoff voltage of 3.0 V at a C-rate range of 1–10 C after the abovementioned optimized CC-CV charging mode. As demonstrated in Fig. 4e, the TCC pouch cell provides limited capacity at a high discharge rate of 4 C after being fully charged at 4 C (15 min of charging). During this process, both the charge resistance and lithium-ion transport kinetic contributed to large overpotentials, thereby sacrificing the capacity of the TCC case. In comparison, the PCC pouch cell shows a much lower decay rate. Even at 5 C discharge, the discharge capacity of PCC remained 52.2%

after 5 C charging (12 min of charging). Figure 4f,g shows the charge and discharge curves of the multilayer pouch cells with TCC and PCC during the fast discharge scenario. It is evident that the overpotential of the PCC case is much smaller than that of the TCC case, as reflected in the charge–discharge plateau position at the same C rate.

The tolerance of Li^0 plating revealed by DPS in real time

As previously discussed, when charging at extremely fast rates, large overpotentials can cause the Li^+ intercalation potential to drop below the Li/Li^+ equilibrium potential. This triggers the formation of Li^0 plating on the surface of the anode. The presence of plated lithium could react violently with the electrolyte and lead to the formation of 'dead lithium', reduced Coulombic efficiency, and rapid loss of capacity. Additionally, the Li^0 dendrites can penetrate the separator and cause internal short circuits, posing severe safety risks[32]. Recently, we have successfully demonstrated a differential pressure sensing (DPS) technique to precisely monitor the occurrence of Li^0 plating during fast charging[33]. By measuring the real-time change in cell pressure per unit of charge (dP/dQ) and comparing it with a defined threshold based on the maximum dP/dQ during Li^+ intercalation into the negative electrode, we can capture the Li^0 plating event before it grows extensively. To gain a better understanding of how the PCC affects Li^0 plating during fast charging, we combined multilayer NMC|Graphite pouch cells with DPS. This allows us to monitor the Li^0 plating event in real time during operation.

We assembled multilayer PCC and TCC pouch cells and initially activated them at a C/20 rate for two cycles. Afterwards, the cells were stacked with a wood force-distribution plate and a pressure sensor and clamped into a bench vice at a fixed thickness (Fig. 5a and Supplementary Fig. 17a). The cells were then charged using the previous optimal CC-CV protocol, with the total CC-CV time controlled and discharged at 1 C until the voltage reached 3.0 V (Fig. 5b and Supplementary Fig. 17b). During this process, the real-time cell pressure was simultaneously recorded (Fig. 5c and Supplementary Fig. 17c). The change of pressure behaviour was correlated to the charge–discharge behaviour of the pouch cells, which was primarily dominated by the volume change of graphite[33]. The base pressure, i.e., the pressure after full discharge, can serve as an indirect indicator of Li^0 plating. The formation of 'dead Li' and residual SEI increases the irreversible thickness of the anode, resulting in a residual pressure increase after each cycle. The stable base pressures of TCC and PCC pouch cells are below 2 and 5 C, respectively, suggesting that there is no occurrence of Li^0 plating. However, if the base pressure increases as the C rates are further increased (>2 C for TCC and >5 C for PCC), this indicates that the residual SEI and 'dead lithium' have formed and accumulated as a consequence of Li^0 plating.

We conducted further analysis and plotted the differential pressure $dP/|dQ|$ of TCC and PCC pouch cells to study the Li^0 plating behaviour (Fig. 5d,e). The threshold for Li^0 plating was established by picking the maximum dP/dQ observed at low C rates. We chose the maximum dP/dQ established at 1 C for the PCC case and 0.5 C for the TCC case due to their similar SOCs after charging. Resting processes after charge and discharge were excluded in data analysis.

From the charge rate of 1 C (1 h of charging) and 4 C (15 min of charging), the $dP/|dQ|$ of the PCC case remained within the region below the threshold (blue region), indicating that the anode underwent Li^+ intercalation reactions (Supplementary Fig. 18). However, when the charging rate increased to 5 C or higher, the $dP/|dQ|$ curve exceeded the threshold and entered the upper Li^0 plating region (orange region), indicating the occurrence of Li^0 plating. This phenomenon became more pronounced at a higher rate of 10 C (6 min charging). As demonstrated in Fig. 5f, the peak $dP/|dQ|$ below 4 C remained in the Li^+ intercalation region for PCC case. In contrast, Li^0 plating events started to occur much earlier at a charging rate of 3 C (20 min charging) in the TCC case (Fig. 5g). In TCC cells, the maximum $dP/|dQ|$ increased from 3 to 6 C and then decreased from 8 to 10 C, mainly due to the charge process going directly to the CV step at 8–10 C. Therefore, no obvious CC part of the TCC cells was observed at such high C rates.

Extension of PCC

Although PCC cells have a significantly higher tolerance for Li^0 plating compared to TCC cells, it is important to note that Li^0 plating tolerance cannot be directly correlated to our 'quadrupling' concept. The rate of lithium intercalation into graphite primarily influences Li^0 plating, which is different from the DLC in our design. To validate this, we performed simulations of the DLCs in both TCC and PCC cells, as shown in Supplementary Fig. 19. At the rate of DLC, lithium depletion occurs at the surface of the current collector in the TCC case, while it occurs in the middle of electrode in the PCC case. We observed that the DLC of the PCC cell is approximately 3.75 times that of the TCC cell. Under the high DLC of PCC cells, Li^0 could already have deposited on the surface of the anode due to the high overpotential originating from high-rate charging.

Apart from fast charging, PCC design also holds great potential for enhancing the areal loading of batteries, resulting higher battery energy without compromising rate performance. Therefore, it is possible to achieve an energy density of approximately 287 Wh kg^{-1}, while still maintaining the theoretical charging rates of batteries (Supplementary Fig. 20). This innovative PCC design represents a significant departure from the traditional battery structure that has been used for the past three decades. It shows great promise for advancing the design of energy storage devices, offering high energy density and high-rate capability. We anticipate that the incorporation of a tab-less design[26,34] could further boost the rate performance of this design in the future. By slightly altering the way of electrode coating, this new battery design maintains the maximum compatibility with the existing battery manufacturing methods and facilitates the implementation of the tab-less design in the near future. Furthermore, introducing PCC to replace the separators would help alleviate local current density and promote more uniform reactions with the battery system (Supplementary Fig. 21).

Conclusions

In summary, we first conceptualized a PCC for high-energy and fast-charging batteries. This design allows for the simultaneous passage of Li^+ ions through both the PCC and separator, reducing the effective Li^+ transport path length by one half without compromising the electrode thickness. As a result, the DLC capability of high-energy batteries can be quadrupled. This PCC consists of a three-layered, hierarchical and porous polymer matrix with Cu and Al coating on either side. Experiment results demonstrate that multilayer pouch cells equipped with this PCC provides remarkable rate capabilities: 4 C (15 min charging, from 0 to 78.3% SOC), 6 C (10 min charging, from 0 to 70.5% SOC) and 10 C (6 min charging, from 0 to 54.3% SOC), while maintaining a high areal loading of 3 mAh cm^{-2} and a specific energy of approximately 276 Wh kg^{-1} at the whole battery level. Furthermore, this PCC design exhibits improved tolerance to Li^0 plating up to 5 C, enhancing the reversibility and safety of LIBs under fast charging. The advantages offered by the PCC over TCC designs have the potential to enrich battery configurations and could have broad effects on the fast-charging capabilities for next-generation energy storage devices.

Methods

Numerical modelling simulations

The theoretical framework of the numerical model is established on the basis of the work by Newman et al.[35]. Specifically, a pseudo-2-dimensional model is used to simulate the electrochemical response of the porous electrodes. The charge equilibrium within the electrodes is governed by,

$$\nabla \cdot \mathbf{i}_c = 0\,, \tag{2}$$

where $\mathbf{i}_c$ is the electric current density in the electrodes, as defined by Ohm's law,

$$\mathbf{i}_c = -K_c \nabla \phi_s, \tag{3}$$

where K_c represents the electric conductivity and ϕ_s represents the electric potential of an NMC cathode or graphite anode. The solid diffusion of Li^+ in the NMC and graphite active particles is governed by Fick's law,

$$\begin{aligned} \frac{\partial C_s}{\partial t} + \nabla \cdot \mathbf{J}_s = 0, \\ \mathbf{J}_s = -D_s(\nabla C_s), \end{aligned} \tag{4}$$

where $\mathbf{J}_s$ is the Li^+ flux in the active particles and D_s is the Li^+ diffusivity in the active particles.

The charge equilibrium and mass transport in the electrolyte is described by the concentrated electrolyte theory. The charge equilibrium in the electrolyte is,

$$\nabla \cdot \mathbf{i}_l = 0, \tag{5}$$

where $\mathbf{i}_l$ is the electric current in the electrolyte, which is governed by the Li^+ diffusion and migration, as expressed by

$$\mathbf{i}_l = (-K_l \nabla \phi_l) + \frac{2K_l RT}{F}\left(1 + \frac{\partial \ln f}{\partial \ln C_l}\right)(1 - t_+)\nabla \ln C_l, \tag{6}$$

where ϕ_l represents the potential buildup in the electrolyte, K_l represents the ionic conductivity of the electrolyte, C_l represents the Li^+ concentration of in the electrolyte, R represents the gas constant, T represents the temperature, F represents Faraday's constant, t_+ represents the transference number of Li^+ and f represents the mean molar activity coefficient of the electrolyte. The relationship between the charge transfer rate (i) and the overpotential (η) is described by the Butler–Volmer equation.

$$i = i_0\left(\exp\left(\frac{\alpha_a F\eta}{RT}\right) - \exp\left(-\frac{\alpha_c F\eta}{RT}\right)\right), \tag{7}$$

where α_a (α_c) is the transfer coefficient of anodic (cathodic) reactions, i_0 is the exchange current density and η is the overpotential of the charge transfer reactions, as described by

$$\eta = \phi_s - \phi_l - \phi_{eq}, \tag{8}$$

where ϕ_{eq} represents the equilibrium potential for the (de)lithiation of the NMC or graphite active materials. The exchange current density i_0 is expressed by,

$$i_0 = F(k_c)^{\alpha_a}(k_a)^{\alpha_c}(C_{s\_max} - C_s)^{\alpha_a}(C_s)^{\alpha_c}\left(\frac{C_l}{C_{l\_ref}}\right)^{\alpha_a}, \tag{9}$$

where k_c (k_a) denotes the rate constants of the anodic (cathodic) reactions, C_s is the Li^+ concentration in the active materials, C_{s_max} is the maximum Li^+ concentration in the active materials and C_{l_ref} is a reference Li^+ concentration of the electrolyte. The mass transport of Li^+ in the electrolyte is described by,

$$\begin{aligned} \frac{\partial C_l}{\partial t} + \nabla \cdot \mathbf{J}_l = 0, \\ \mathbf{J}_l = -D_l \nabla C_l + \frac{\mathbf{i}_l t_+}{F}, \end{aligned} \tag{10}$$

where $\mathbf{J}_l$ is the Li^+ flux in the electrolyte and D_l is the Li^+ diffusivity in the electrolyte. The effective transport properties of the porous electrodes are revised as $D_{eff} = \frac{\varepsilon}{\tau} D_{bulk}$, where D_{eff} is the effective transport properties (such as Li-ion diffusivity and ion conductivity), D_{eff} is the intrinsic transport properties of the liquid electrolyte, τ is the tortuosity of the electrodes, and ε is their porosity.

The simulations were conducted using COMSOL Multiphysics software. For a detailed exposition of the modelling approach, readers are referred to a preceding publication[22]. The geometric, physical and electrochemical parameters used in the simulation are consistent with the experiments (Supplementary Table 1). Two battery configurations are used in the simulation: the six-layered batteries with the TCC and the PCC. For the PCC configuration, six repeat units of separator–anode–PCC–cathode are assembled. The PCC unit is set as the same as the separator with electrolyte with a porosity of 40%. For both the TCC and PCC configuration, the cathode thickness is fixed to 70 µm for 3.0 mAh cm^{-2}, with a N/P ratio of 1.1. Two areal capacities of the cathode are simulated: 3.0 and 9.0 mAh cm^{-2}, with a N/P ratio of 1.1. The galvanostatic charging using different C rates, calculated on the basis of the cathode areal loading. The current densities applied on the cathode side are calculated according to different C rates. Other parameters such as the porosity, transference number, diffusivity and tortuosity are shown in the Supplementary Table 1.

Resistance simulation

Calculation for electrical resistance was performed for the model of a typical cylindrical LIB, i.e., 18650 LIBs. In the case of the TCC, the widths and thicknesses of the current collectors were 54 mm and 12 µm for the cathode (Al), and 57 mm and 8 µm for the anode (Cu), respectively. In the case of the PCC, a 1.5 µm thick conductive layer was used for both the cathode and anode. Regarding the electrical conductivities, measured values of 4.67×10^7 and 5.6×10^7 S m^{-1} were used for anodes of the PCC and TCC, while for cathodes, 3.14×10^7 and 3.77×10^7 S m^{-1} were used for the PCC and TCC, respectively.

PCC fabrication

A bullet-proof and porous paper-type aramid film (Kevlar) with a thickness of 15 µm and a high nanosized porosity of 65% was used as the main substrate polymer for the PCC. Microporous polymide with tuneable pore sizes were coated on either side of the Kevlar based on an inverse phase separation to form the hierarchical PCC matrix (Supplementary Methods). Porous PVDF-HFP can be also served as the microporous layer in the PCC matrix. PVDF-HFP (molecular weight ~455,000) was first dissolved in acetone (10 wt%), and then different water content amounts (0, 5, 10 and 15 wt%) were slowly added to create a blend precursor slurry. The slurry was then used to coat both sides of a commercial separator or Kevlar film at room temperature. The rapid evaporation of the acetone and water mixture facilitates the phase separation of PVDF-HFP, leading to the formation of a microporous structure. The sample was then dried in the vacuum oven at 60 °C for 2 days before use.

The obtained PCC matrix was further pretreated with O_2 plasma for 5 min to enhance the surficial adhesion for metal coating. Porous conductive Cu and Al layers were deposited on the two sides of above porous polymer substrate by a pulsed d.c. magnetron sputtering with a pressure less than 10^{-6} torr and argon used as protective gas.

Electrode fabrication

Both cathode and anode composite electrodes were prepared via a conventional slurry-casting method. A segregated carbon nanotube (CNT) dispersion (Tuball, catalogue no. OCSiAl) that consisted of 0.4 wt% single wall carbon nanotube and 2 wt% binders (polyvinylidene difluoride) in *N*-methyl-2-pyrrolidone, battery active materials (NMC or graphite) and carbon black (Timcal C45 carbon) was used as additives.

For anodes, the CNT dispersion (including binder) was mixed with graphite powder (Superior Graphite catalogue no. SLC1506T) and carbon black. As a specific amount of binder was already included in the CNT dispersion, there was no need to add additional binder.

The mass fraction of graphite/CNT mass fraction/carbon black/binder in the resultant electrodes was controlled to 86/2/2/10% by controlling the mass ratio. For instance, 25 ml of the CNT dispersion was mixed with 4.2 g of graphite, 100 mg of carbon black and 400 mg of butyl benzyl phthalate santicizer to obtain an electrode with 2 wt% CNTs. The slurry was then cast onto the polyethylene terephthalate (PET) sides of the PET/aluminium (PET/Al) film. The electrode was then dried in an oven at 70 °C overnight, followed by a vacuum drying at 60 °C for 2 days, then dried in an oven at 120 °C overnight to remove the residual solvent. By changing the gap of the doctor blade, electrodes with various thickness could be obtained. The dried electrode was then peeled off from the PET/Al film by bending. The free-standing electrode was cut into a specific area size and placed on the Cu foil (Cu TCC) or the Cu side of the PCC for calendaring.

For the cathodes, we used NMC (Toda America, Inc.) to mix with the CNT dispersion and carbon black. The mass fraction of active materials/CNT mass fraction/carbon black/binder in the resultant electrodes was controlled to 92/1/2/5%. Typically, 25 ml of CNTs were ground together with 9.2 g of NMC, 300 mg carbon black and 400 mg butyl benzyl phthalate santicizer to obtain an electrode with 1.0 wt% CNT. The slurry was then cast on the PET side of PET/Al film as the anode electrode. The electrode was released from the PET/Al film by bending and dried in the same manner as the anode. The free-standing cathode electrode was cut into a specific area size and placed on the Al foil (Al TCC) or the Al side of the PCC for calendaring.

Battery assembly

NMC|graphite multilayer pouch cells were assembled with electrodes with Cu|Al TCC and the above fabricated PCC. As illustrated in Supplementary Fig. 22, another two edge electrodes were co-operated to balance the capacity of the PCC pouch cell. In the TCC pouch cell, all the anode current collectors were connected to a nickel tab while all the cathode current collectors were connected to an Al tab. In the PCC pouch cell, all the Cu metal sides of the PCC were connected to a strip of Cu foil (1 cm width) by a welding machine before being connected to a nickel tab, while all the Al metal sides of the PCC were connected to a strip of Al foil (1 cm width) and then connected to an Al tab. A polypropylene-polyethylene-polypropylene (Celgard 2325) porous film was used as the separator for both TCC and PCC pouch cells. $LiPF_6$ (1.2 M) in ethylene carbonate/ethyl methyl carbonate (EC/EMC, 3/7 in weight) with 2 wt% fluoroethylene carbonate (Sigma Aldrich) was used as the electrolyte for full-cell measurements. The electrolyte usage in the pouch cells was 10 g Ah^{-1}. The overall capacities of the pouch cells with the TCC and PCC were controlled to be the same. Therefore, the dimensions (in inches) of the TCC cathode, TCC anode, PCC cathode and PCC anode were 3.30 × 3.30 cm (1.30 × 1.30), 3.56 × 3.56 cm (1.40 × 1.40), 2.92 × 2.92 cm (1.15 × 1.15), and 3.18 × 3.18 cm (1.25 × 1.25), respectively. Battery cycling was performed on a land tester with a current up to 5 A. Both the TCC and PCC pouch cell were first activated for two cycles by charging to 4.2 and discharging to 3.0 V at a current density of 0.05 C. The pouch cells were then charged by CC (to 4.2 V) and constant voltage (holding at 4.2 V) until the total charging time reached a specific value according to its charging rate (1 h for 1 C, 30 min for 2 C and so forth), then discharged at the same C rate of 1 C. For a fast charge–discharge protocol, the charge protocols were kept the same, while the discharge rates were set to CC discharge from 1 to 10 C until the voltage reached 3 V. A 5 min resting time was added to each end of the charge and discharge step.

Material characterization

The in-plane electrical conductivity of the PCC and TCC was measured using a four-point probe technique. Four parallel contact lines were then deposited on the electrode surface using silver conductive paste. The morphology and microstructure of the samples were examined by field emission SEM (using an Apreo S LoVac Scanning Electron Microscope, Thermo Fisher Scientific) in high-vacuum mode with an acceleration voltage of 5 keV. Mechanical measurements were conducted from free-standing samples using a Instron 5565 tensile tester (100 N load cell) at a strain rate of 0.5 mm min^{-1}. The contact angle measurement was conducted on the Rame–Hart 290 contact angle goniometer. The ionic conductivity was performed by electrochemical impedance spectroscopy in Biologics VMP3 with the frequency ranging from 1 to 100 MHz. Cyclic voltammetry was measured by Biologics VMP3 with a scan rate of 0.5 mV s^{-1} and voltage window of 0–5 V. The shape of electrode was made by an ultraviolet light laser cutter with a wavelength of 355 nm (model no. 3530-30, diode-pumped solid state-included the Samurai marking system) or guillotine paper cutter.

Operando pressure testing

A wood block (length × width × height, 5 × 5 × 2.5 cm (in inches, 2 × 2 × 1)) was attached to the pouch cell as a force-distribution plate, which was larger than the cell core. The activated multilayer pouch cell was clamped into a bench vice with a pressure setup (LBC-500, Transducer Techniques). The setup was rested for 6 h before testing. Pressure data collection and battery cycling were initiated and started at the same time.

Data availability

The data that support the findings of this study have been included in this article and its Supplementary Information. Source data are provided with this paper.

References

1. Crabtree, G. The coming electric vehicle transformation. *Science* **366**, 422–424 (2019).
2. Viswanathan, V. et al. The challenges and opportunities of battery-powered flight. *Nature* **601**, 519–525 (2022).
3. Schäfer, A. W. et al. Technological, economic and environmental prospects of all-electric aircraft. *Nat. Energy* **4**, 160–166 (2019).
4. Yang, X.-G., Liu, T., Ge, S., Rountree, E. & Wang, C.-Y. Challenges and key requirements of batteries for electric vertical takeoff and landing aircraft. *Joule* **5**, 1644–1659 (2021).
5. Deng, J., Bae, C., Denlinger, A. & Miller, T. Electric vehicles batteries: requirements and challenges. *Joule* **4**, 511–515 (2020).
6. Liu, Y., Zhu, Y. & Cui, Y. Challenges and opportunities towards fast-charging battery materials. *Nat. Energy* **4**, 540–550 (2019).
7. Tomaszewska, A. et al. Lithium-ion battery fast charging: a review. *eTransportation* **1**, 100011 (2019).
8. Li, G. Regulating mass transport behavior for high-performance lithium metal batteries and fast-charging lithium-ion batteries. *Adv. Energy Mater.* **11**, 2002891 (2021).
9. Gallagher, K. G. et al. Optimizing areal capacities through understanding the limitations of lithium-ion electrodes. *J. Electrochem. Soc.* **163**, A138 (2015).
10. Mao, C., Ruther, R. E., Li, J., Du, Z. & Belharouak, I. Identifying the limiting electrode in lithium ion batteries for extreme fast charging. *Electrochem. Commun.* **97**, 37–41 (2018).
11. Logan, E. & Dahn, J. Electrolyte design for fast-charging li-ion batteries. *Trends Chem.* **2**, 354–366 (2020).
12. Li, J. et al. Methyl acetate as a co-solvent in NMC532/graphite cells. *J. Electrochem. Soc.* **165**, A1027 (2018).
13. Yang, X.-G. et al. Asymmetric temperature modulation for extreme fast charging of lithium-ion batteries. *Joule* **3**, 3002–3019 (2019).
14. Yang, X.-G., Zhang, G., Ge, S. & Wang, C.-Y. Fast charging of lithium-ion batteries at all temperatures. *Proc. Natl Acad. Sci. USA* **115**, 7266–7271 (2018).
15. Ye, Y. et al. Cold-starting all-solid-state batteries from room temperature by thermally modulated current collector in sub-minute. *Adv. Mater.* **34**, 2202848 (2022).

16. Heubner, C., Schneider, M. & Michaelis, A. Diffusion-limited C-rate: a fundamental principle quantifying the intrinsic limits of li-ion batteries. *Adv. Energy Mater.* **10**, 1902523 (2020).
17. Newman, J. Optimization of porosity and thickness of a battery electrode by means of a reaction-zone model. *J. Electrochem. Soc.* **142**, 97 (1995).
18. Paul, P. P. et al. A review of existing and emerging methods for lithium detection and characterization in Li-ion and Li-metal batteries. *Adv. Energy Mater.* **11**, 2100372 (2021).
19. Feng, X., Ren, D., He, X. & Ouyang, M. Mitigating thermal runaway of lithium-ion batteries. *Joule* **4**, 743–770 (2020).
20. Zhu, P. et al. A review of current collectors for lithium-ion batteries. *J. Power Sources* **485**, 229321 (2021).
21. Yang, Y. et al. Quantification of heterogeneous degradation in Li-ion batteries. *Adv. Energy Mater.* **9**, 1900674 (2019).
22. Xu, R. et al. Heterogeneous damage in Li-ion batteries: experimental analysis and theoretical modeling. *J. Mech. Phys. Solids* **129**, 160–183 (2019).
23. Ebner, M., Chung, D. W., García, R. E. & Wood, V. Tortuosity anisotropy in lithium-ion battery electrodes. *Adv. Energy Mater.* **4**, 1301278 (2014).
24. Yang, X.-G., Leng, Y., Zhang, G., Ge, S. & Wang, C.-Y. Modeling of lithium plating induced aging of lithium-ion batteries: transition from linear to nonlinear aging. *J. Power Sources* **360**, 28–40 (2017).
25. Yan, K. et al. Selective deposition and stable encapsulation of lithium through heterogeneous seeded growth. *Nat. Energy* **1**, 16010 (2016).
26. Choudhury, R., Wild, J. & Yang, Y. Engineering current collectors for batteries with high specific energy. *Joule* **5**, 1301–1305 (2021).
27. Ye, Y. et al. Ultralight and fire-extinguishing current collectors for high-energy and high-safety lithium-ion batteries. *Nat. Energy* **5**, 786–793 (2020).
28. Pegel, H., Wycisk, D. & Sauer, D. U. Influence of cell dimensions and housing material on the energy density and fast-charging performance of tabless cylindrical lithium-ion cells. *Energy Storage Mater.* **60**, 102796 (2023).
29. Park, S.-H. et al. High areal capacity battery electrodes enabled by segregated nanotube networks. *Nat. Energy* **4**, 560–567 (2019).
30. Song, M. & Choe, S.-Y. Fast and safe charging method suppressing side reaction and lithium deposition reaction in lithium ion battery. *J. Power Sources* **436**, 226835 (2019).
31. Vikrant, K., McShane, E., Colclasure, A. M., McCloskey, B. D. & Allu, S. Quantification of dead lithium on graphite anode under fast charging conditions. *J. Electrochem. Soc.* **169**, 040520 (2022).
32. Liu, F. et al. Dynamic spatial progression of isolated lithium during battery operations. *Nature* **600**, 659–663 (2021).
33. Huang, W. et al. Onboard early detection and mitigation of lithium plating in fast-charging batteries. *Nat. Commun.* **13**, 7091 (2022).
34. Tranter, T. G., Timms, R., Shearing, P. R. & Brett, D. Communication—prediction of thermal issues for larger format 4680 cylindrical cells and their mitigation with enhanced current collection. *J. Electrochem. Soc.* **167**, 160544 (2020).
35. Doyle, M., Fuller, T. F. & Newman, J. Modeling of galvanostatic charge and discharge of the lithium/polymer/insertion cell. *J. Electrochem. Soc.* **140**, 1526 (1993).

Acknowledgements

This work is supported by Murata Manufacturing Co., Ltd. S.T.O. acknowledges support from the TomKat Center Fellowship for Translational Research at Stanford University. We thank the Stanford Nano Shared Facilities and the Stanford Nanofabrication Facility for the SEM, contact angle, tensile strength characterizations and Lesker sputter fabrication. We thank Dupont for providing the porous Kevlar film.

Author contributions

Y.Y. and Y.C. conceived the concept. R.X., Y.M. and T.Y. performed the COMSOL simulation. W.H., F.L. and T.L. helped with the battery pressure testing and analysis. H.A., W.Z., J.O.A., A.C., Z.C., X.X., Z.Z., Y.P. and S.T.O. assisted with electrochemical experiments. Y.W. carried out the electronic conductivity measurement. X.G., H.K., R.M., Y.S., Y.M., T.Y. and Y.N. helped with the device fabrication, simulation and data analysis. Y.Y. and Y.C. wrote the paper. W.Z., R.A.V. and Y.C. revised the paper. All the authors contributed to the discussion of the results.

Competing interests

H.K., Y.S., R.M., Y.M., T.Y. and Y.N. are employed by Murata Manufacturing Co., Ltd. The other authors declare no competing interests.

Additional information

Supplementary information The online version contains supplementary material available at https://doi.org/10.1038/s41560-024-01473-2.

Correspondence and requests for materials should be addressed to Yi Cui.

Peer review information *Nature Energy* thanks Leif Nyholm and the other, anonymous, reviewer(s) for their contribution to the peer review of this work.

Reprints and permissions information is available at www.nature.com/reprints.